

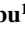




Exploring the Predictability of the High-Energy Tail of MEE Precipitation Based on Solar Wind Properties

J. A. Salice¹ , H. Nesse¹ , E. M. Babu¹ , C. Smith-Johnsen¹ , and I. G. Richardson^{2,3} 

¹Birkeland Centre for Space Science, Department of Physics and Technology, University of Bergen, Bergen, Norway,

²Heliophysics Science Division, NASA Goddard Space Flight Center, Greenbelt, MD, USA, ³Department of Astronomy, University of Maryland, College Park, MD, USA

Key Points:

- The solar wind parameter ϵ best predicts the peak flux of the >292 keV electron precipitation independent of solar wind structure
- The delay in the peak flux of >292 keV electron precipitation relative to that of >43 keV electrons is influenced by solar wind speed
- On average, electron precipitation >292 keV persists 2–3 days longer than electron precipitation >43 keV

Correspondence to:

J. A. Salice,
Josephine.Salice@uib.no

Citation:

Salice, J. A., Nesse, H., Babu, E. M., Smith-Johnsen, C., & Richardson, I. G. (2023). Exploring the predictability of the high-energy tail of MEE precipitation based on solar wind properties. *Journal of Geophysical Research: Space Physics*, 128, e2022JA031194. <https://doi.org/10.1029/2022JA031194>

Received 29 NOV 2022

Accepted 1 MAR 2023

Abstract Medium Energy Electron (MEE) precipitation (≥ 30 keV) ionizes the mesosphere and initiates chemical reactions, which ultimately can reduce mesospheric and stratospheric ozone. Currently, there are considerable differences in how existing parameterizations represent flux response, timing, and duration of MEE precipitation, especially considering its high-energy tail (≥ 300 keV). This study compares the nature of ≥ 300 to ≥ 30 keV electron fluxes to better understand differences within MEE precipitation. The MEE fluxes are estimated from measurements by the Medium Energy Proton and Electron Detector (MEPED) onboard the Polar Orbiting Environmental Satellite (POES) from 2004 to 2014. The fluxes are explored in the context of solar wind drivers: corotating high-speed solar wind streams (HSSs) and coronal mass ejections (CMEs) alongside their associated solar wind properties. Three key aspects of ≥ 300 keV electron fluxes are investigated: maximum response, peak timing, and duration. The results reveal a structure-dependent correlation (0.89) between the peak fluxes of ≥ 30 and ≥ 300 keV electrons. The epsilon coupling function correlates well (0.84) with the ≥ 300 keV peak flux, independent of solar wind structure. The ≥ 300 keV flux peaks 0–3 days after the ≥ 30 keV flux peaks. The highest probability ($\sim 42\%$) occurs for a 1-day delay, while predictive capabilities increase when accounting for solar wind speed. The ≥ 300 keV flux response has the highest probability of lasting 4 days for both CMEs and HSSs. The results form a base for a stochastic MEE parameterization that goes beyond the average picture, enabling realistic flux variability on both daily and decadal scales.

Plain Language Summary Electrons with energies >30 keV precipitating into the Earth's atmosphere is known as medium energy electron (MEE) precipitation. Solar wind properties drive the rate and energy of MEE. MEE precipitation is a relevant solar forcing as it produces ozone-depleting substances. Variations in ozone concentration can modify the atmospheric temperature profile and lead to changes in atmospheric circulation that can map down onto surface climate. The community's capability of parameterizing MEE precipitation is an active field of research. This study aims to build a foundation for an MEE parameterization that represents realistic variability on daily and decadal scales by exploring the variability in the context of different solar wind properties. The study focuses on three key aspects regarding the differences within the energy spectrum of MEE precipitation: maximum response, timing, and duration. The key aspects are evaluated regarding the probability of a specific response. This study looks at an entire solar cycle (11 yr). It is found that solar wind properties, such as solar wind speed, can help determine the probability of a particular MEE response. The results from this paper will be key elements for constructing an MEE precipitation parameterization to be applied in a chemistry-climate model.

1. Introduction

Energetic particle precipitation (EPP) causes chemical changes in the upper atmosphere (≥ 50 km), for example, by creating NO_x and HO_x gasses (e.g., Smith-Johnsen et al., 2017; Verronen & Lehmann, 2013; Verronen et al., 2006; Zawedde et al., 2018). The increase of NO_x is particularly significant due to its long lifetime during high-latitude winter darkness, allowing for downward transportation and depletion of stratospheric ozone (Damiani et al., 2016; Maliniemi et al., 2021; Solomon et al., 1982). Ozone plays a significant role in stabilizing the atmosphere's radiation balance and climate system by absorbing incoming solar radiation and emitting long-wave infrared radiation. Hence, variation in ozone will cause changes in the atmospheric temperature profile and lead to changes in atmospheric circulation that can potentially map down onto surface climate (Baldwin & Dunkerton, 2001; Kidston et al., 2015; Maliniemi et al., 2016; Seppälä et al., 2016). The strengths of the

© 2023 The Authors.

This is an open access article under the terms of the [Creative Commons Attribution-NonCommercial License](https://creativecommons.org/licenses/by-nc/4.0/), which permits use, distribution and reproduction in any medium, provided the original work is properly cited and is not used for commercial purposes.

atmospheric ionization rates and chemical modulation highly depend on the number, energy, and type of particles hitting the atmosphere.

EPP consists of both protons and electrons. Auroral electron ($\lesssim 30$ keV) and proton ($\lesssim 1$ MeV) precipitation originating from the plasma sheet will ionize the lower thermosphere and upper mesosphere. Medium energy electrons (MEEs; $\gtrsim 30$ keV) from the radiation belts deposit their energy throughout the upper mesosphere, whereas the high-energy tail of MEE ($\gtrsim 300$ keV) can reach the upper stratosphere (Turunen et al., 2009). Occasionally, high-energetic precipitating protons from solar proton events (SPEs; 1–50 MeV) can ionize the stratosphere, where the production of NO_x and HO_x allows for a direct impact on stratospheric ozone (Jackman et al., 2005; Tyssøy & Stadsnes, 2015; Tyssøy et al., 2013; Zawedde et al., 2018).

The link between electron precipitation at auroral energies and how it affects NO_x in the lower thermosphere is well established (Marsh et al., 2004; Sinnhuber et al., 2011). Similarly, the effects of SPEs are fairly well quantified (Funke et al., 2011; Jackman et al., 2005; Tyssøy & Stadsnes, 2015; Tyssøy et al., 2013). However, knowledge gaps remain regarding the MEE precipitation spectrum, particularly when considering the high-energy tail. MEE precipitation is acknowledged as one of the relevant factors in understanding stratospheric ozone depletion (Matthes et al., 2017). Currently, the community's capability of parameterizing MEE precipitation is an active field of research (Babu et al., 2022; Beharrell et al., 2015; Duderstadt et al., 2021; Mironova et al., 2019; Partamies et al., 2021; Pettit et al., 2019; Tyssøy et al., 2019; Tyssøy, Partamies, Babu, Smith-Johnsen, & Salice, 2021; Tyssøy et al., 2021; van de Kamp et al., 2018, 2016). Instrumental challenges and different data handling result in a wide range of electron flux and ionization rate estimates (Tyssøy et al., 2021). This uncertainty propagates into chemistry-climate model projections of the associated chemical effects (Sinnhuber et al., 2022).

Geomagnetic indices are often used as proxies for precipitation. The lower part of the electron precipitation spectrum is known to correspond well with geomagnetic indices (e.g., Hendrickx et al., 2015; Østgaard et al., 2002; Y. Zhang & Paxton, 2008). The high-energy tail of MEE precipitation is more ambiguous (Turunen et al., 2009; Tyssøy, Babu, Smith-Johnsen, & Salice, 2021). The Coupled Model Intercomparison Project Phase 6 (CMIP6) provides climate projections in a multi-model context (WCRP, 2011). The current CMIP6 solar forcing recommendation utilizes van de Kamp et al. (2016)'s daily resolved model for MEE precipitation (Matthes et al., 2017). The model is based on the 0° Medium Energy Proton and Electron Detector (MEPED) measurements onboard the NOAA Polar Orbiting Environmental Satellites (POES) and is scaled by the Ap index. Several limitations to this approach have been established (e.g., Mironova et al., 2019; Pettit et al., 2019; Tyssøy et al., 2019; Tyssøy et al., 2021).

Tyssøy et al. (2019) find that the Ap-based model falls short in reproducing flux levels, variability associated with strong geomagnetic storms, and the duration of storms. Typically, the high-energy tail of MEE acts differently compared to the lower energies with respect to the timing (Østgaard et al., 2017) and duration (Longden et al., 2008) of the flux response. Moreover, as the parameterization developed in van de Kamp et al. (2016) is based on an average response to geomagnetic activity, it is likely to downplay the impact of extreme events (Tyssøy et al., 2021). To model the effect of the transient forcing of MEE on the atmosphere, a correct representation of the daily MEE variability over a wide range of energies with respect to both the background drizzle and storm periods is necessary. Additionally, an average representation of the typical storm might not reflect the variability throughout a solar cycle. In particular, the solar wind drivers of MEE exhibit a fairly strong solar cycle dependence (e.g., Asikainen & Ruopasa, 2016; Kilpua, Balogh, et al., 2017; Kilpua, Koskinen, et al., 2017), potentially causing a systematic bias on decadal scales (Tyssøy et al., 2019). An accurate representation of MEE precipitation will allow for better parameterization on both daily and decadal scales.

The solar wind fuels the magnetospheric processes that accelerate and scatter electrons trapped in the radiation belts. Coronal mass ejections (CMEs) and high-speed solar wind streams (HSSs) are the primary large-scale heliospheric solar wind structures driving geomagnetic disturbances (e.g., J. Zhang et al., 2007). These structures occasionally occur in rapid sequences or are merged, leading to intense geomagnetic disturbances (Asikainen & Ruopasa, 2016; Kilpua, Balogh, et al., 2017; Kilpua, Koskinen, et al., 2017). CMEs consist of various components such as shocks, sheaths, ejecta, and clouds (for reviews on CMEs, see e.g., Kilpua, Balogh, et al., 2017; Kilpua, Koskinen, et al., 2017; Zurbuchen & Richardson, 2006). HSSs are often accompanied by a corotating interaction region (CIR) leading the stream (for a review on HSSs and CIRs, see Richardson, 2018). Generally, CMEs tend to be brief (~ 1 day) and may include strong, slowly varying magnetic field components, while HSSs tend to last longer and have fluctuating magnetic field components (e.g., Borovsky & Denton, 2006; Kataoka &

Table 1

Nominal Detector Responses in the Three Electron Channels E1, E2, and E3 of the SEM-2 MEPED Electron Detector (Evans & Greer, 2004) and the New Optimized Integral Energy Limit for the Different Channels (Ødegaard et al., 2017)

Energy channel	Nominal lower limit [keV]	New optimized lower limit [keV]
E1	>30	>43
E2	>100	>114
E3	>300	>292

Miyoshi, 2006; Kilpua, Balogh, et al., 2017; Kilpua, Koskinen, et al., 2017). Throughout a solar cycle, HSSs are nearly always (except at solar maxima) more frequent than CMEs (Asikainen & Ruopsa, 2016). The fundamentally different solar wind properties drive different geomagnetic disturbances as well as different MEE precipitation characteristics (e.g., Borovsky & Denton, 2006; Longden et al., 2008).

This study explores daily MEE precipitation in the context of its solar wind drivers and the associated solar wind properties, such as solar wind speed and interplanetary magnetic field (IMF). Notably, the focus is on the behavior of the high-energy tail compared to low-energy MEE precipitation. The low-energy MEE is generally easier to quantify due to its high correspondence to geomagnetic activity in contrast to the high-energy tail. The MEE

bounce loss cone (BLC) fluxes are estimated based on observations from MEPED onboard POES/METOP over 11 yr from 2004 to 2014. Periods of isolated CME- and HSS-driven solar wind structures and periods when they are in close sequence are examined. Three key aspects of ≥ 300 keV electron flux are investigated:

- The maximum flux response.
- The timing of the maximum flux response.
- The duration of the flux response.

The key aspects are evaluated regarding the probability of a specific response. The goal is to identify variables that increase the accuracy of a daily MEE parameterization to be applied in a chemistry-climate model. This paper is organized as follows: Section 2 describes the data and methods used, Section 3 presents the results which are discussed in Section 4, and finally, conclusions of this study are provided in Section 5.

2. Data and Method

2.1. MEE Flux

The series of NOAA/POES and EUMETSAT/MetOp satellites are Sun-synchronous, low-altitude polar-orbiting spacecraft. The spacecraft circle at ~ 850 km altitude with a period of ~ 100 min, resulting in 14–15 orbits per day (Evans & Greer, 2004). The MEPED instrument is mounted on the POES series and three of the MetOp spacecraft. The combined measurements from the different satellites give a near-continuous observation of MEE precipitation from 1979 until today.

MEPED consists of a set of eight separate solid-state particle detector systems. Two are proton solid-state detector telescopes, two are electron solid-state detector telescopes, and the remaining four are omni-directional detector systems for high-energy protons measured over a wide range of angles (Evans & Greer, 2004). The electron detectors monitor the intensity of electrons in three bands from 30 to 2,500 keV (Evans & Greer, 2004). The nominal electron energy limits for the electron telescope in the three bands E1, E2, and E3 as given in Evans and Greer (2004) are listed in Table 1. When in operation, the true electron energy limits depend on the incoming electron energy spectrum (Yando et al., 2011). The new optimized effective integral energy limits and associated geometric factors are based on a series of realistic power laws and exponential spectra and were determined by Ødegaard et al. (2017) by applying the geometric factors given in Yando et al. (2011).

The electron solid-state detector telescopes consist of a 0° and 90° telescope. The 0° telescope is oriented radially outward along the Earth-satellite connecting axis. The 90° telescope is perpendicular to the 0° telescope and anti-parallel to the satellite's velocity vector. Both telescopes are rotated away from the described axis by 9° to ensure a clear field of view (Evans & Greer, 2004). Charged particles gyrate along the magnetic field lines. The angle between the velocity vector of a particle and the magnetic field line is known as the particle's pitch angle. This angle determines whether the particle will be lost to the atmosphere or mirrored back along the magnetic field. The atmospheric BLC is defined as the range of pitch angles at which particles will be lost. The size of the BLC changes with latitude and longitude due to variations in the magnetic field strength. In MEPED, the 0° telescopes will mainly measure atmospheric BLC particles when traveling across high geomagnetic latitude, while the 90° telescopes will mainly measure particles at the edge or outside of the BLC (Rodger et al., 2010).

Separately, the two telescopes do not give an accurate estimate of the BLC electron flux (Tyssøy et al., 2016) as the 90° telescope will give an overestimation and the 0° telescope an underestimation. This is because the

energetic electron fluxes are often strongly anisotropic with decreasing fluxes toward the center of the BLC (Tyssøy et al., 2016). Tyssøy et al. (2016) estimated a complete BLC flux for each electron energy channel by combining measurements from both telescopes with electron pitch angle distributions from theories of wave-particle interactions in the magnetosphere. The Focker-Planck equation for particle diffusion (Kennel & Petschek, 1966; Theodoridis & Paolini, 1967) is solved for a wide range of diffusion coefficients. The solutions are then transformed to the satellite altitude and stored in a look-up table. The ratio between the fluxes detected by the 0° and 90° detector is compared to the theoretical solution considering the telescope's viewing directions relative to the magnetic field. Finally, the size of the BLC is predicted based on the International Geomagnetic Reference Field model and is applied to estimate the precipitating fluxes. The BLC flux estimate is done separately for each energy channel, as the level of particle diffusion will vary with energy. A detailed explanation of the method can be found in Tyssøy et al. (2016).

This study applies the BLC fluxes with the new optimized effective integral limits E1 (>43 keV) and E3 (>292 keV). The BLC fluxes represent daily fluxes averaged over 55°–75° corrected geomagnetic (CGM) latitude and all magnetic local times for a full solar cycle from 2004 to 2014. During this period, up to seven satellites have been operational, all with the newest instrument package SEM-2. More details of the operating satellites and data coverage for the specific time period can be found in Babu et al. (2022) and Tyssøy, Partamies, Babu, Smith-Johnsen, and Salice (2021). For simplicity, >43 and >292 keV electron fluxes will be referred to as E1 and E3, respectively.

2.2. Solar Wind Structure and Parameters

The near-Earth solar wind is divided into three basic flow types:

- Corotating high-speed streams that originate from coronal holes at the Sun.
- Transient flows associated with CMEs at the Sun.
- Slower, interstream solar wind typically associated with the streamer belt at the Sun.

Classification of these three structures for every day of the 11 yr period from 2004 to 2014 was made using the same methods discussed by Richardson and Cane (2012). Their list of daily resolution solar wind structures, based on a 1 hr resolution assessment of these structures, includes the day the structure starts to the day it ends, even if that solar wind structure did not predominately occur on these days. The classifications are based on a variety of data, including near-Earth solar wind parameters from the OMNI database, geomagnetic activity data, and energetic (~0.1–100 MeV) particle and cosmic ray observations (Richardson & Cane, 2012). Since the near-Earth solar wind data is essentially continuous throughout the investigated period, Richardson and Cane (2012)'s classifications are considered representative and suitable for this study.

The corotating high-speed streams, denoted as HSSs in this paper, typically have solar wind speed $v \gtrsim 450$ km/s and include both the high-speed stream and CIR where the leading edge of the high-speed stream interacts with the preceding slower, cooler, and denser solar wind. The transient flows originating with CMEs at the Sun include interplanetary CMEs (ICMEs), the manifestations in the solar wind of the CMEs, and the associated upstream shocks and post-shock/sheath regions (Richardson & Cane, 2012). Richardson and Cane (2012) refer to ICMEs and their upstream shocks and sheaths collectively as “CME-associated” structures. This paper follows the same approach and, for brevity, uses “CME” to refer to these structures. More information on the respective data sets and how the different structures are identified can be found in Richardson and Cane (2012) and references therein.

The solar wind magnetic field strength and direction as well as the solar wind speed are primary drivers of geomagnetic activity. In this paper, the IMF component B_z (in GSM-coordinates) and plasma flow speed, v , were retrieved from the OMNI 2 database with a daily resolution from 2004 to 2014. In addition, the epsilon parameter, ϵ , which is based on B_z and v and which gives a general idea of the energy transfer between the solar wind and the magnetosphere, was retrieved from the SuperMAG database (Gjerloev, 2012) with daily resolution over the same time interval. ϵ is given by:

$$\epsilon = \frac{4\pi}{\mu_0} v B^2 \sin^4\left(\frac{\theta}{2}\right) l_0^2 \quad (1)$$

Equation 1 is based on Akasofu (1981) and is given in SI units (Watt) by Koskinen and Tanskanen (2002). In Equation 1, $4\pi/\mu_0 = 10^7$, v is solar wind velocity, B is the magnitude of the solar wind magnetic field, θ is the clock angle (the angle between geomagnetic north and the projection of the IMF in the plane transverse to the radial direction), and l_0 is seven times the Earth's radius ($l_0 = 7R_E$).

The current parameterization for MEE precipitation recommended for CMIP6 is represented as daily averages based on daily Ap values (Matthes et al., 2017). Moreover, the high-energy tail of the MEE spectra often peaks after 1–2 days (Ødegaard et al., 2017; Tyssøy, Partamies, Babu, Smith-Johnsen, & Salice, 2021). Because of this, the goal of our study is not to attempt to understand the role of solar wind drivers over short time intervals but to reveal their stochastic role in the behavior of precipitating the high-energy tail of MEE. Tyssøy, Partamies, Babu, Smith-Johnsen, and Salice (2021) demonstrate that the MEE precipitating fluxes are determined by accumulated geomagnetic activity. As such, it is not the specific short periods of negative B_z or positive ϵ that determine the daily MEE precipitation. Hence, we apply daily averages of the hourly determined solar wind structures, the 1 min B_z , v , and ϵ parameters alongside daily averaged MEE fluxes.

2.3. Method

In this study, CMEs and HSSs are categorized into single and combined events. The combinations of events include a CME followed by an HSS and vice versa. In the 11 yr of interest, 420 events were selected based on the requirements that they were classified as a structure for at least 1 day and had slower, interstream solar wind the day before and after. However, 12 events were removed because of gaps in the electron flux data. Additionally, 52 events with fluxes falling below 250 electrons/($\text{cm}^2 \cdot \text{s} \cdot \text{sr}$) were removed because they were close to the detectors noise level of around 100 electrons/($\text{cm}^2 \cdot \text{s} \cdot \text{sr}$). Moreover, 107 events, where either E1 or E3 reached their highest flux before the solar wind event, were removed. These events would have given misleading flux responses, as this study evaluates the electron fluxes within the solar wind structure and does not consider pre-event fluxes. Based on these criteria, 249 events within the 11 yr period were retained: 34 CMEs, 181 HSSs, 17 CME + HSSs, and 17 HSS + CMEs.

Figure 1 shows a superposed epoch analysis (SEA) over a 14-day period of E1 and E3 as well as the parameters B_z , v , and ϵ for all 249 events, denoted as the Base. The onset is defined by the peak in E1. Previous studies have shown that the E1 evolution and maximum flux response are fairly well correlated with geomagnetic activity (Tyssøy, Partamies, Babu, Smith-Johnsen, & Salice, 2021; van de Kamp et al., 2016). The evolution of E1 and the three solar wind parameters in Figure 1 confirms this correlation. Hence, this study targets the behavior of the E3 peak relative to the E1 peak and, therefore, defines the onset based on E1. In addition, choosing the flux peak instead of flux rise avoids the pitfall of MEE radiation belt fluxes being subject to adiabatic variability where it is not always evident when the flux rise starts (Ødegaard et al., 2017). Moreover, the peak flux is a pragmatic parameter to apply in a model assuming a fairly consistent rise time. In this study, the peak fluxes refer to the highest flux response within the solar wind structure period.

Figure 1 captures the long duration of elevated fluxes, particularly for E3. Note that other events may occur during the 8 days following onset, which can give rise to some of the features in the SEA. When evaluating the E3 peak, as well as the delay between E1 and E3, activity throughout the 8-day period after the onset does not affect the interpretations. However, when evaluating the duration, events with activity throughout the 8-day period after the onset are discarded (see Section 3.4).

Under the assumption that it is the accumulated effect of solar wind drivers that is responsible for E3 characteristics, we apply a 4-day average of the three parameters B_z , v , and ϵ from 2 days before the onset (−2 days) to 1 day after (+1 day). This captures the main energy transfer period as illustrated by ϵ in the lower panel of Figure 1, which occurs before the average E3 peak. The respective time interval is optimized and confirmed based on regression analysis between E3 and different time intervals for ϵ . Note that B_z averages out around zero as it oscillates between negative and positive values throughout the day. A daily average will not capture the oscillation but can still indicate if B_z was more negative or positive throughout the day and if large negative values occur.

SEAs of the flux response in the E1 (black) and E3 (green) flux channels during the different events are presented in Figure 2. The top panel shows Base events and gives a general picture of how active solar wind periods affect electron precipitation. The four subsequent panels show the flux evolution during CMEs, HSSs, CME + HSSs, and HSS + CMEs. As HSSs make up ~73% of all the events, they will correspond well with the Base. All five panels list the E1 and E3 peaks with the associated timings. In addition, the transition between structures within the combined events is marked on the upper x -axis. Note that one HSS + CME event does not change from an HSS-driven structure to a CME-driven one until after the plotted period of 8 days from onset. This event is not disregarded as we do not differentiate between electron fluxes reaching their peak in a certain structure of the combined events.

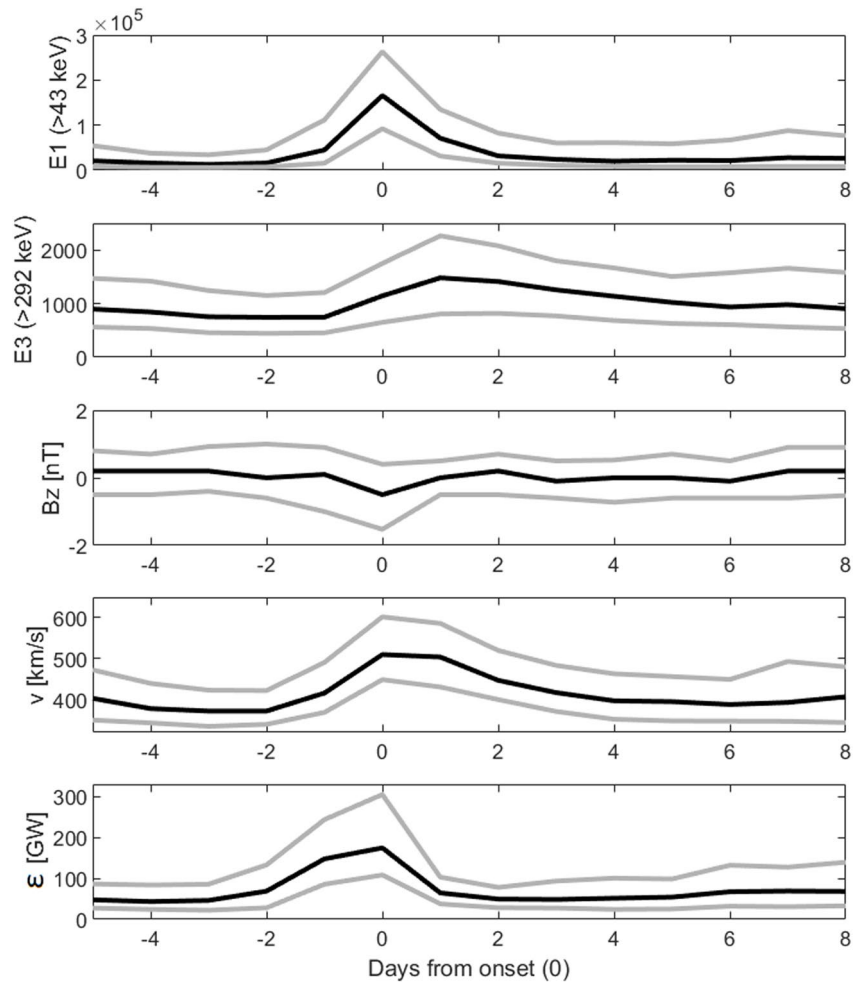


Figure 1. Superposed epoch analysis of the evolution of parameters for all events in this study (Base). From the top: E1 (>43 keV), E3 (>292 keV), B_z , v , and ϵ . The fluxes are in $\text{cm}^{-2}\text{s}^{-1}\text{sr}^{-1}$. The onset is defined as the E1 maximum flux response within the solar wind structure period (denoted as the E1 peak). The gray lines show the lower and upper quartiles.

The electron flux channels E1 and E3 represent two different energy intervals within the MEE range, the latter being the high-energy tail. As the magnetospheric acceleration and scattering processes are energy-dependent (Millan & Thorne, 2007), it is expected that the nature of particles precipitating at these two energy intervals also differs. The E1 maximum response is higher as it not only represents an integral spectrum but naturally has a higher flux due to the flux always decreasing with higher energy. However, it is evident that the broadness of the E1 and E3 peaks typically differs. A prolonged E3 response implies a significant accumulated effect. More time is needed to accelerate and scatter electrons at higher energies (>292 keV) which can lead to a delay in the E3 response compared to that of E1 (Ødegaard et al., 2017; Tyssøy, Partamies, Babu, Smith-Johnsen, & Salice, 2021). As solar wind drives the acceleration and scattering processes of electrons in the magnetosphere, this study will examine to which degree different solar wind structures generate different characteristic flux responses in the high-energy tail (E3) of MEE precipitation.

3. Results

3.1. The General Flux Evolution

The average flux evolution presented in Figures 1 and 2 represents an overview of the data used in this study. The figures demonstrate the expected differences between the two energy channels of MEE precipitation. Both Figures 1 and 2 show that the E3 peak is typically about two orders of magnitude smaller than that of E1. From

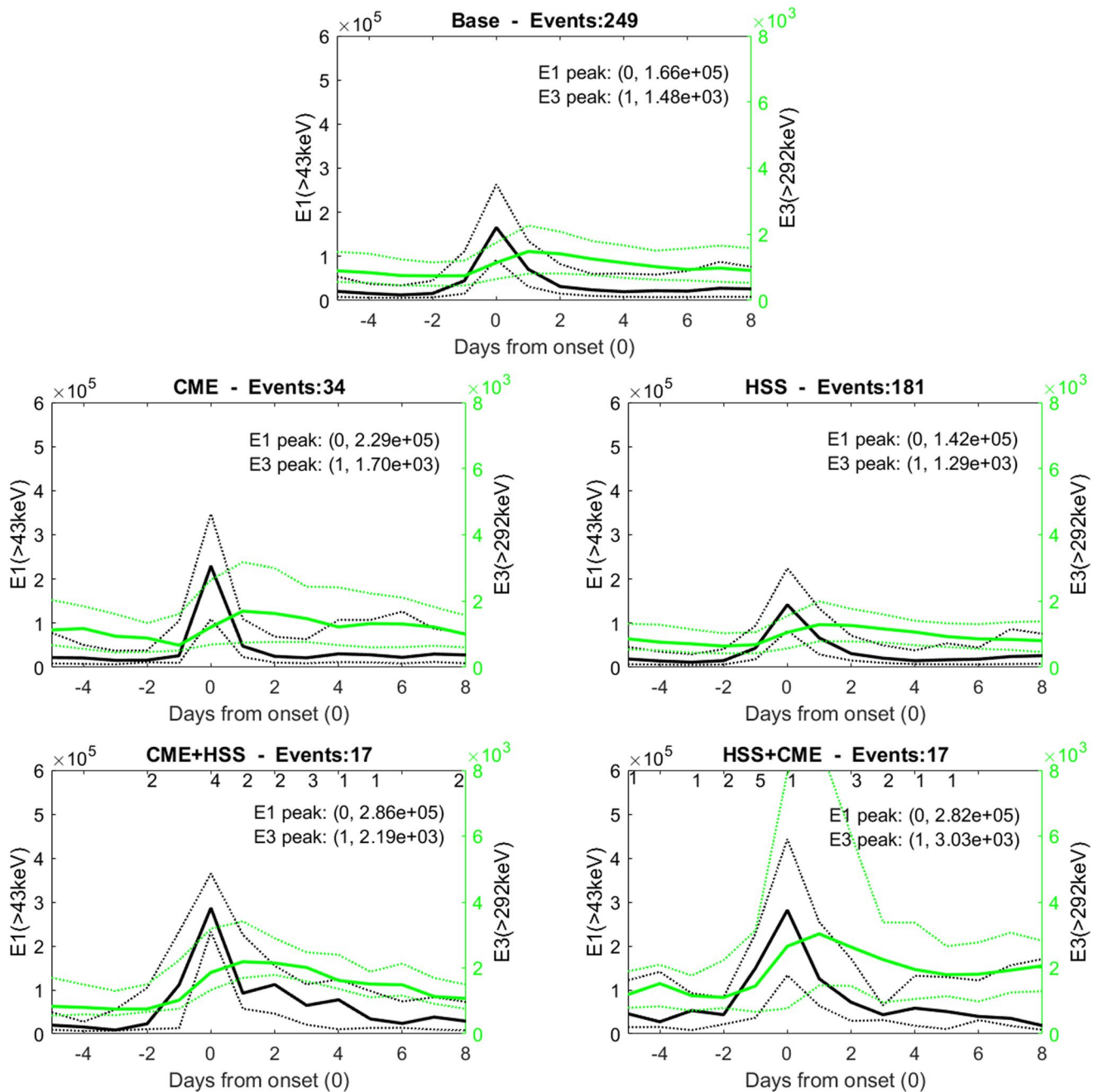


Figure 2. SEAs of the electron flux for the E1 (>43 keV) (black) and E3 (>292 keV) (green) energy channels during different solar wind structures given in $\text{cm}^{-2}\text{s}^{-1}\text{sr}^{-1}$. The x-axis indicates days from the onset defined as in Figure 1. The dotted lines show the lower and upper quartiles. The coordinates of the E1 and E3 peaks are presented in the upper right corner. The numbers at the top of the bottom two panels indicate the number of events with a structural solar wind change on a specific day. Note that the y-axis scaling of the black and green curves are different; the green y-axis is on the right-hand side. However, the y-axes are the same for all panels.

Figure 2, the average HSS has considerably lower flux responses than other structures. The two combined structures have higher E1 and E3 average peaks than single structures. HSS + CMEs show large variability in E3 as the upper and lower quartiles indicate extremely high and low flux responses, respectively. E3 typically has the highest flux responses within 1 day after the E1 peak. Also evident is the relatively steep rise and fall of E1 around the onset compared to the broader E3 response. The following results explore potential prediction capabilities for the E3 peak, the delay of the E3 peak relative to that of E1, and the duration of E3 enhancement in relation to solar wind properties.

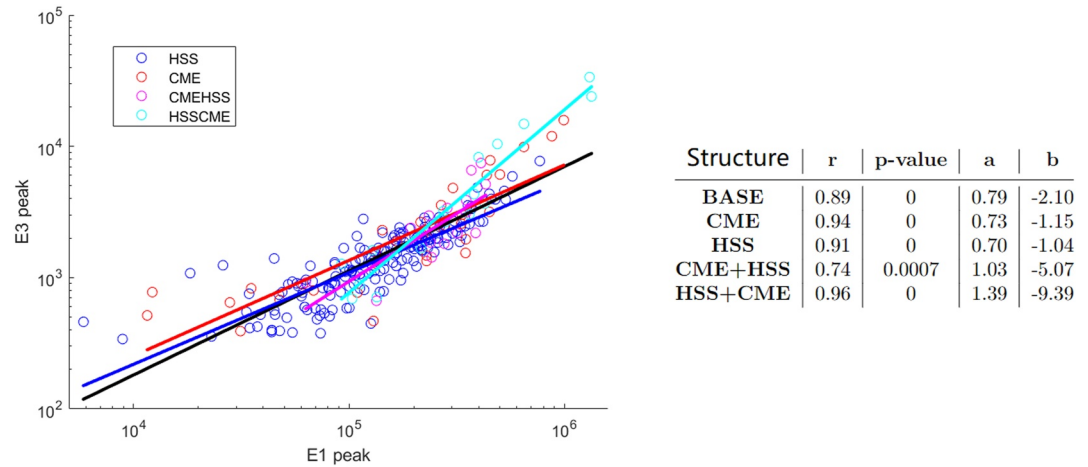


Figure 3. Scatter plot of the dependence the E3 (>292 keV) peak has on the E1 (>43 keV) peak. The two fluxes are given in $\text{cm}^{-2}\text{s}^{-1}\text{sr}^{-1}$. The regression lines for the different structures, including the base (black), are plotted on top. The fluxes are on a log-log scale. The correlation coefficients (r), the statistical significance values (p -value), and the line fitting parameters, a and b , for the different structures are shown in a table to the right.

3.2. The E3 (>292 keV) Peak Flux

Figure 3 shows a log-log scatter plot of how the E3 peak depends on the peak of E1. On the right is a table of the correlation coefficients (r), p -values, and line-fitting parameters a and b . Note that the peak fluxes refer to the maximum flux response within the solar wind structure period. The E3 peak scales consistently to that of the E1 peak with a correlation coefficient of 0.89 for all events (Base). Independently, the solar wind structures also have high correlation coefficients (>0.90), with the exception of CME + HSSs, which have a correlation coefficient of 0.74. CMEs and HSSs have similar rates of change (≈ 0.70), while the rate of change for the combined structures is higher (>1.00). The E3 peak during HSS + CMEs has a significantly stronger sensitivity to changes in the E1 peak with a rate of change equal to 1.39. For high E1 values ($>3 \times 10^5 \text{cm}^{-2}\text{s}^{-1}\text{sr}^{-1}$), Figure 3 shows that the fit derived from the Base events would underestimate the strong HSS + CME response due, particularly, to the dominance of the weaker HSS response.

Figure 4 shows the same as Figure 3 just for how the E3 peak depends on different solar wind properties. From top to bottom, the solar wind properties are B_z , v , and ϵ . The properties are averaged over 4 days, from 2 days before to 1 day after onset. As in Figure 3, the correlation between the peak fluxes and the solar wind parameters is portrayed in a scatter plot with the corresponding linear regression lines for each structure. Note that the B_z and v plots are semi-log plots while ϵ is a log-log plot. To the right of each scatter plot is a table with the same content as in Figure 3.

When considering the Base presented in Figure 4, B_z (top panel) and v (middle panel) correlate poorly with the E3 peak as the correlation coefficients are -0.51 and 0.49 , respectively. However, the correlation between the Base and ϵ (bottom panel) is high (0.84). ϵ has small p -values (<0.05) and the highest correlation coefficients (r) for the various solar wind structures. An exception is found for CMEs where the correlation coefficient between solar wind speed and E3 is higher (0.75). The relation between the ϵ coupling function and the E3 peak (bottom panel) shows that the rates of change for the different structures are fairly similar, and the lines are nearly superposed. In fact, CMEs and HSSs have the same rate of change (1.16).

The poor correlation between E3 and B_z (top panel in Figure 4) might be due to the negative and positive variations in B_z being averaged over 4 days, whereas it is the negative B_z periods that would most effectively impact E3.

3.3. The Delay of E3

To utilize the correlations presented in Figures 3 and 4, information on the difference in timing between the two peak fluxes is needed. Figure 5 shows the probability of a given delay in the E3 peak for the different structures.

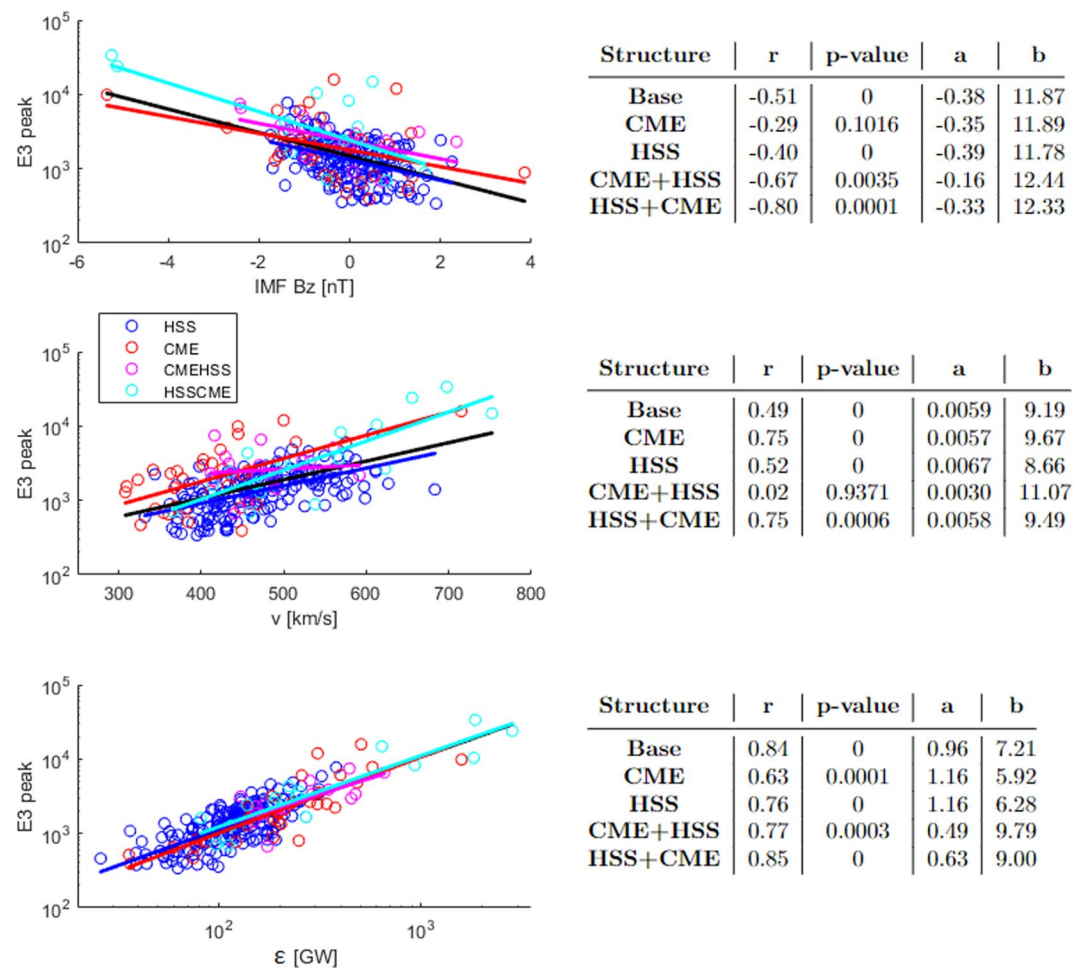


Figure 4. Scatter plots of the dependence the E3 (>292 keV) peak [$\text{cm}^{-2}\text{s}^{-1}\text{sr}^{-1}$] has on the 4-day averaged IMF B_z (top), v (middle), and ϵ (bottom). The regression lines for the different structures, including the Base (black), are plotted on top. B_z and v are on a log-lin scale while ϵ is on a log-log scale. The correlation coefficients (r), the statistical significance values (p -value), and the line fitting parameters, a and b , for the different structures are shown in a table to the right of each plot.

A 0-day delay indicates that E3 peaks within the same day as E1, a 1-day delay that E3 peaks within the following day, and so on. The highest probability is for a 1-day delay of the E3 peak, independent of solar wind structure (see Figure 5). A high probability for a 1-day delay is expected based on the SEAs shown in Figures 1 and 2. However, the delay varies from zero to 3 days. CMEs have the highest probability (32%) for a 0-day delay and the lowest probability for a 3-day delay (9%). Both CME and HSS + CME events have a higher probability (32% and 29%, respectively) for a 0-day delay than a delay of more than 1 day.

All structures have >60% chance for a 1-day delay of the E3 peak. A higher resolution is needed to see differences within these days. Still, based on daily variability, this study targets parameters that influence the timing of the maximum response in E3 from 0 to 3 days.

Figure 6 shows the average B_z , v , ϵ , and E1 peak values for the different delays in the E3 peak for CMEs (red) and HSSs (blue). (The low statistics of the combined structures resulted in large errors and insignificant results, and are therefore not shown here.) In general, none of the parameters show a significant trend in influencing the delay of the E3 peak. Still, a weak tendency is evident in the solar wind speed, where slower speed might be associated with a longer delay.

Figure 7 shows the probabilities of different delays in the E3 peak with regard to solar wind speed. The x -axis indicates the speeds at which the 4-day average v exceeds. The y -axis for the two top panels shows the probability of the indicated delay with a solar wind speed above the given x -value, while the bottom panels show the number

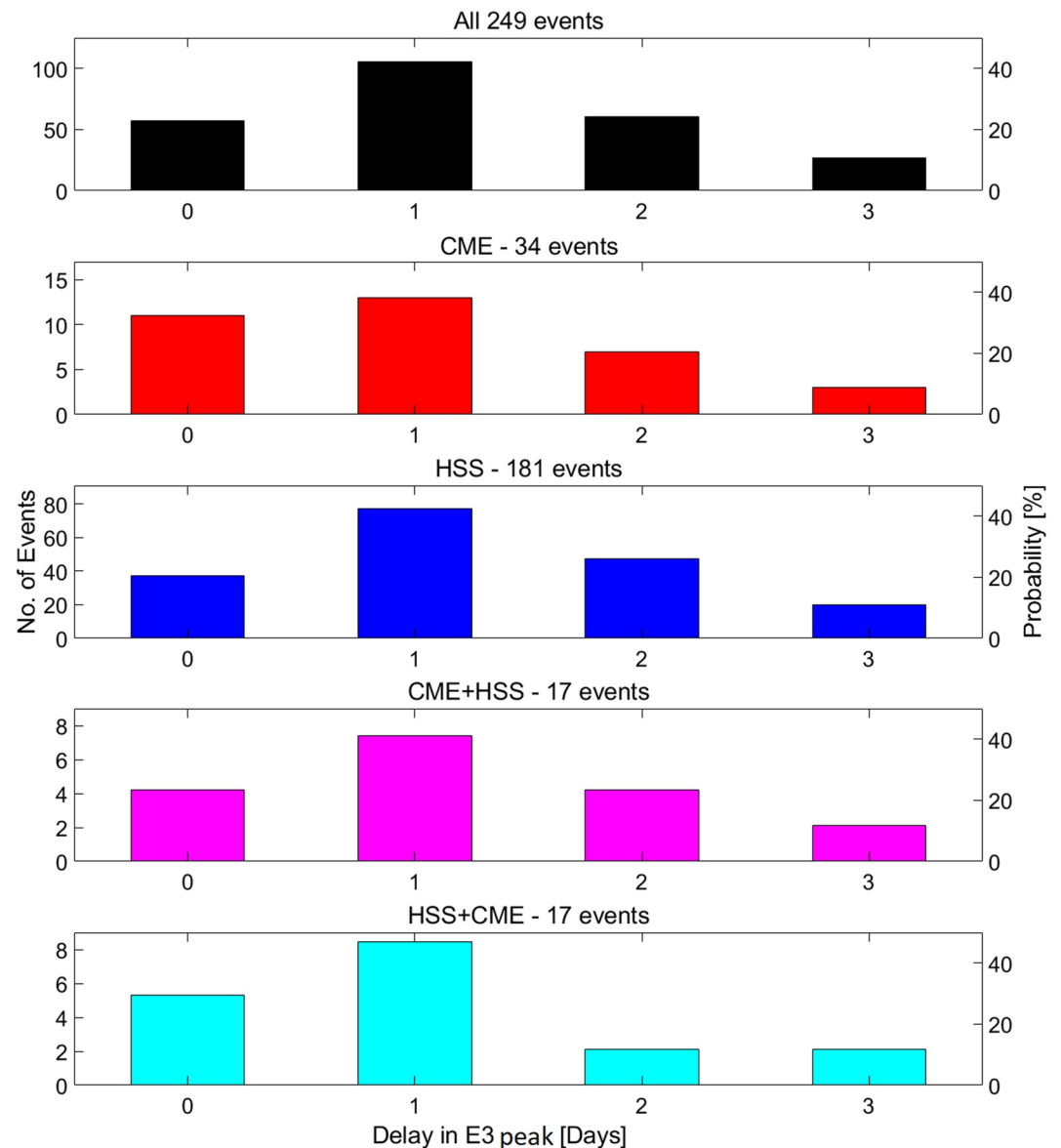


Figure 5. The delay in the E3 (>292 keV) peak relative to the E1 (>43 keV) peak associated with the different solar wind structures showed in days on the x-axis. The left y-axis shows the number of events with a certain E3 delay, and the right y-axis shows the probability of this delay.

of events with an average v above the given x -value. Only results for v are shown as Bz , ϵ , and E1 showed little influence on the delay when examined in the same manner as presented in Figure 7.

Figure 7 shows that there is a threshold in the solar wind speed at $v > 400$ km/s and $v > 550$ km/s for CMEs and HSSs, respectively, above which the probability of a 0-day delay increases substantially. For CMEs, this probability increases from 47% at $v > 400$ km/s to 75% at $v > 475$ km/s, while $v > 350$ km/s reduces the chance of a two- and 3-day delay to below 10%. For HSSs, a 1-day delay is dominant up until ~ 425 km/s, where the probability of a 0-day delay increases consistently and reaches the same probability (41%) of a 1-day delay at $v > 550$ km/s.

3.4. The Duration of the Precipitation Events

To evaluate the duration of the flux responses, the full width at the half-maximum value of the peak for both E1 and E3 was calculated. Twelve events were discarded as E1, E3, or both did not fall below this value within 8 days

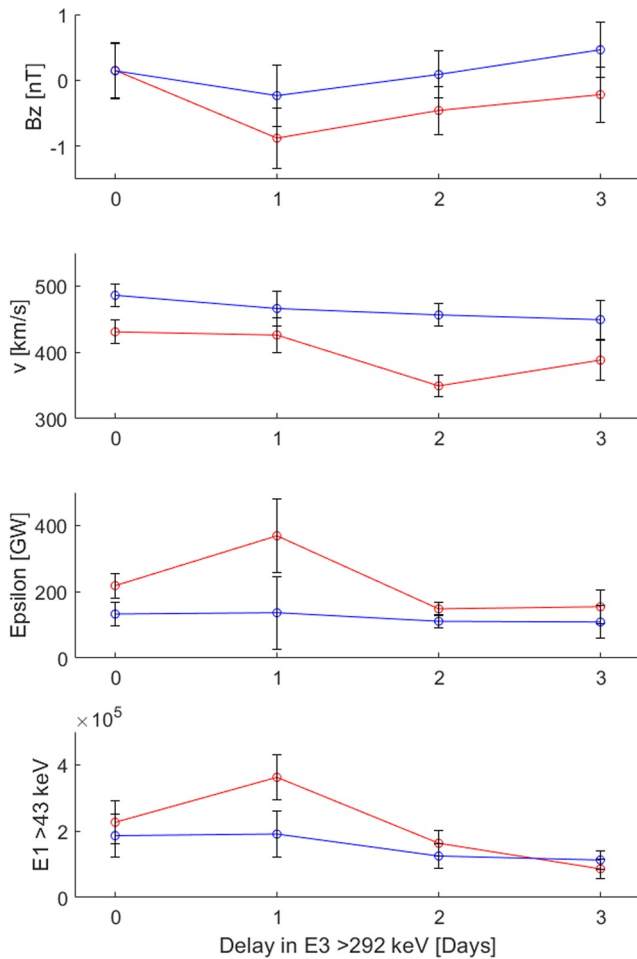


Figure 6. The average B_z , v , ϵ , and maximum $E1 (>43 \text{ keV})$ [$\text{cm}^{-2}\text{s}^{-1}\text{sr}^{-1}$] values associated with the delay of the $E3 (>292 \text{ keV})$ peak for CMEs (red) and HSSs (blue). The error bars show the standard deviations of the average values.

from the onset due to new activity. This led to a loss of 17 HSSs and three HSS + CMEs. The duration of the E1 and E3 responses and their occurrence probability are presented in Figure 8.

Generally, when considering the Base (top), the E3 response lasts longer (>2 days) compared to the duration of the E1 response (<3 days). Figure 8 also shows that CMEs have the highest probability (62%) for an elevated E1 response of just 1 day, while for HSSs, CME + HSSs, and HSS + CMEs, a duration of 2 days is most common. The duration of the high-energy tail (E3) is most likely to last 4 days for both CMEs and HSSs, with a probability of 32% and 23%, respectively. Even though CMEs have a higher probability for a shorter E1 response, the highest probability of the E3 duration is still 4 days. In fact, 79% of CMEs have an E3 duration of 3 days or longer. The combined structures, though having low statistics, also indicate longer flux enhancements of the high-energy tail compared to E1.

No significant tendency was evident between the duration of E3 and B_z , v , or ϵ when examined in the same manner as delay in Figures 6 and 7.

4. Discussion

In this study, the high-energy tail of MEE precipitation has been compared to the E1 response and investigated in the context of solar wind drivers and the associated v , B_z , and ϵ parameters concerning the following features.

- The maximum flux response
- The delay in maximum flux response
- The duration of the flux response

An in-depth understanding of these three key parameters is necessary to represent the entire MEE precipitation spectrum realistically. Evaluating each parameter's potential in determining the probability of a specific response paves the way for understanding which variables can be applied to increase the accuracy of an MEE parameterization on both daily and decadal scales.

4.1. The Maximum Precipitating Fluxes

On average, HSSs have lower MEE flux responses than CMEs and combined structures (see Figure 2). Consistent with our results, Asikainen and Ruopasa (2016) showed that the average precipitating fluxes in 2004–2014 were higher for CMEs compared to HSSs for the E1 and E3 energy channels. The relatively low HSS flux response might be partly because the precipitating MEE flux is averaged over a wide latitude band from 55° to 75°N and the precipitation region associated with HSS typically does not expand as widely as CMEs (Babu et al., 2022). The upper quartile of the MEE flux for HSS + CMEs in Figure 2 demonstrates that these structures can trigger extreme MEE flux levels in both E1 and E3. Kilpua, Balogh, et al. (2017) and Kilpua, Koskinen, et al. (2017) also pointed out the potential of severe geomagnetic storms associated with the combination of solar wind structures. Moreover, Asikainen and Ruopasa (2016) found that the efficiency of both HSSs and CMEs in producing MEE precipitation peaks in the declining phase of the solar cycle, where these events often occur simultaneously or in close sequence.

HSSs are more frequent throughout a solar cycle than CMEs (Asikainen & Ruopasa, 2016) and, in this study, constitute 73% of the identified structures during the investigated 11 yr. As the average HSS has considerably weaker flux responses compared to CME-related events, an MEE parameterization based on “the average event” will underestimate the potentially strong impact associated with CME-related activity and exaggerate flux levels associated with the common HSSs. Hence, such a model will not be able to represent the variability associated with MEE precipitation for daily and decadal scales. Tyssøy et al. (2019) showed that van de Kamp et al. (2016)'s ApEEP model, which is scaled by the geomagnetic index A_p based on median flux responses, falls short in reproducing the flux levels and variability associated with strong geomagnetic storms. Additionally, Tyssøy

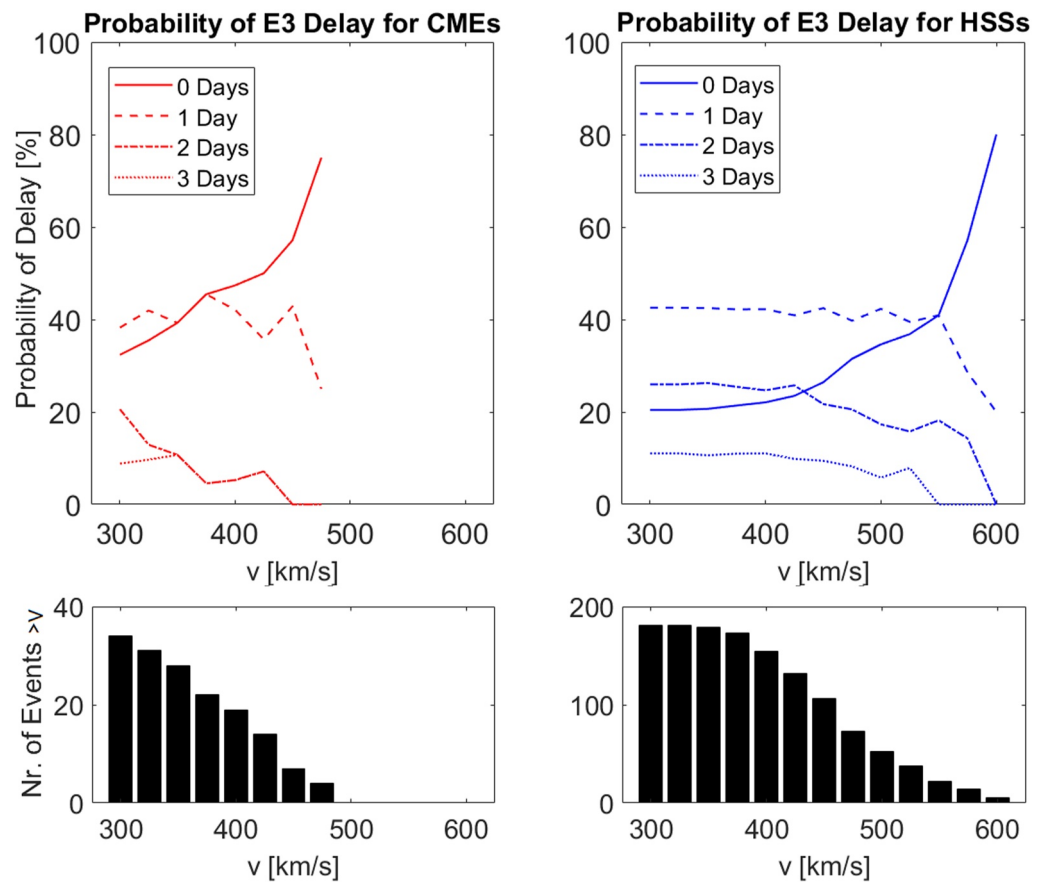


Figure 7. The solar wind speed-dependent probability of the delay in the E3 (>292 keV) peak for CMEs (red) and HSSs (blue). The y-axis of the two top panels shows the probability of the indicated delay dependent on events with average solar wind speeds that exceed the indicated x-axis value. The y-axis of the two bottom panels shows the number of events with average solar wind speeds which exceed the indicated x-value.

et al. (2021) compared eight different ionization rates, all based on MEPED observations, during an active period of March/April 2010, including a period of combined events. The comparison showed that the ApEEP-based model predicts significantly weaker ionization rates than other estimates, particularly when considering the high-energy tail. Hence, a more realistic representation of MEE precipitation might be achieved by considering the probability of flux response variations regarding solar wind structure.

Figure 3 implies that knowledge of the E1 peak will enable the prediction of the peak flux of the high-energy tail as the correlation coefficient for the Base events is 0.89. Independently, the solar wind structures all have a high correlation (>0.90), with the exception of CME + HSSs, which have a low correlation (0.74). The E3 peak during combined structures stands out as it has a stronger sensitivity to changes in E1. Particularly, HSS + CMEs stand out with a significantly higher rate of change of 1.39. As HSSs strongly dominate the average structure, a model based on the average relationship will systematically underestimate the high-energy tail of MEE precipitation during combined events when the E1 response is high ($>3 \times 10^5 \text{ cm}^{-2} \text{ s}^{-1} \text{ sr}^{-1}$).

Figure 4 reveals ϵ as a key parameter to determine the peak of E3, independent of solar wind structure. Ødegaard et al. (2017) reported a linear relationship between the energy input into the magnetosphere and precipitation of relativistic electrons by studying 41 weak and moderate geomagnetic storms driven by CIRs. Our study suggests, however, that this relationship is independent of the driving solar wind structure. This is not self-evident as multiple studies suggest that the energy partitioning within the magnetosphere might be different for different solar wind structures (N. E. Turner et al., 2009).

Note that to utilize the dependency between either the E1 and E3 peaks or the E3 peak and the ϵ parameter in a model, the timing of the flux peaks needs to be known. The timing of the E1 peak corresponds well with the

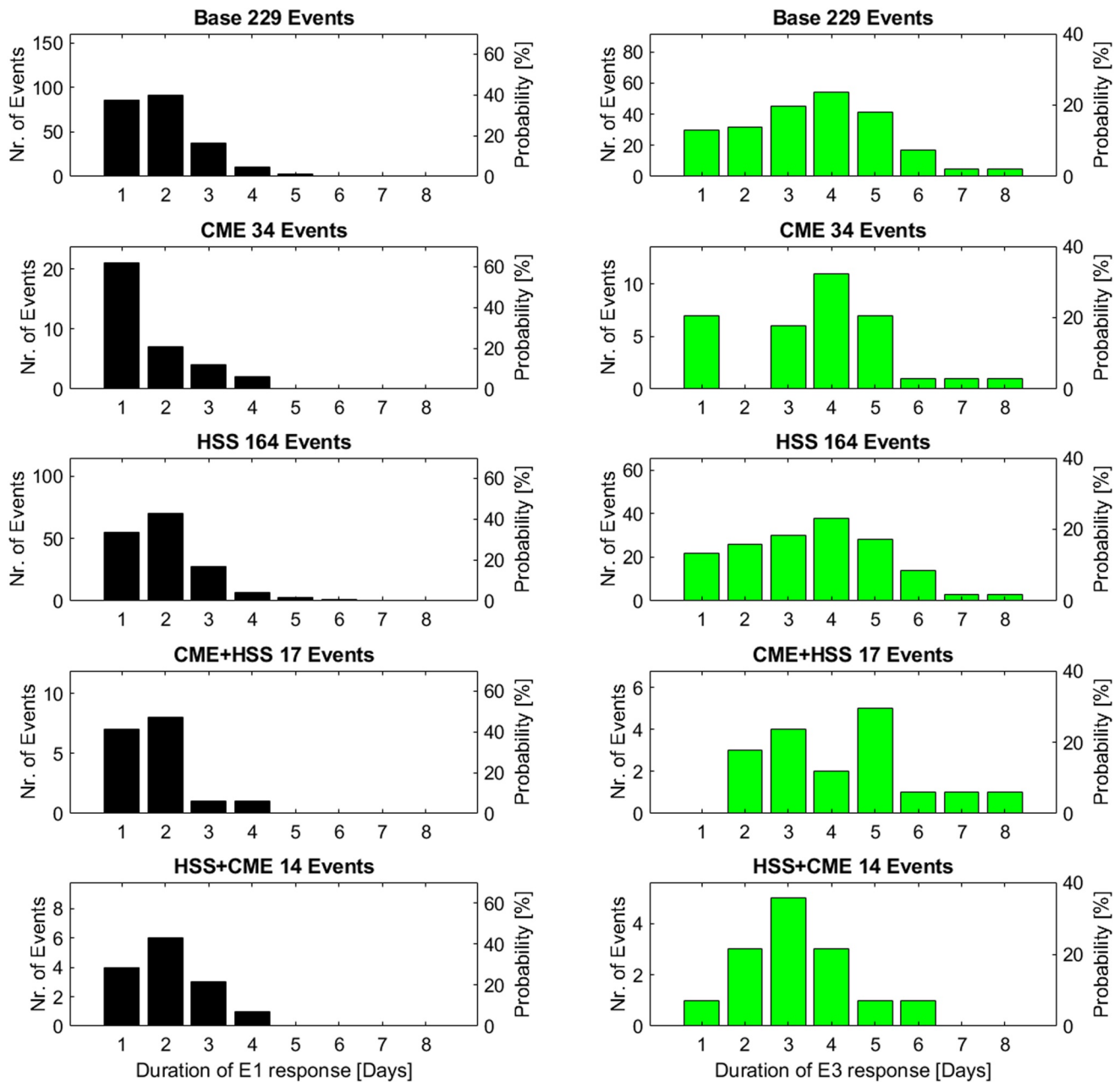


Figure 8. Probability of the duration [days] of E1 (>43 keV) and E3 (>292 keV) for the four different solar wind structures. E1 is presented in black to the left, and E3 in green to the right. From top to bottom, the solar wind structures are Base, CME, HSS, CME + HSS, and HSS + CME.

indices B_z , v , and e (see Figure 1). Previous studies have also shown that the E1 peak and timing are fairly well correlated with geomagnetic activity (Tyssøy, Partamies, Babu, Smith-Johnsen, & Salice, 2021; van de Kamp et al., 2016). However, the timing of the E3 peak differs from that of E1.

4.2. Delay

Figure 5 shows that the E3 peak has the highest probability of occurring 1 day after onset. Evidence of delayed electron flux responses with increasing electron energy has also been documented in other studies (Li et al., 2005; Longden et al., 2008; Ødegaard et al., 2017; Tyssøy, Partamies, Babu, Smith-Johnsen, & Salice, 2021). Li et al. (2005) found solar wind speed to be a dominant controlling parameter for electron energies from 50 keV to 6 MeV. They identified an energy-dependent time shift of approximately 1 day between 50–75 and 225–300 keV,

consistent with our findings. A similar time shift for the MEE high-energy tail was also found by Longden et al. (2008) and Ødegaard et al. (2017). Moreover, Tyssøy, Partamies, Babu, Smith-Johnsen, and Salice (2021) investigated the predictability of the AE index for MEE precipitation. They demonstrated how high predictability could be achieved when accounting for the delayed response of the high-energy tail ($\gtrsim 300$ keV) by accumulating the geomagnetic activity over time, taking into account the electron flux lifetimes.

The presence of a time delay is consistent with the view of electrons in the radiation belts being accelerated to progressively higher energies over time (Horne et al., 2005). Both Horne et al. (2005) and Rodger et al. (2010) observed the delay in trapped electron particle energies and found an energy-dependent time delay.

This study finds a spread of 0–3 days in the delay of the E3 peak. CMEs have higher probabilities for a fast response than the other solar wind structures as the high-energy tail peaks within a day for 71% of the events. In contrast, HSSs are more likely to have a 2-day delayed E3 peak than a 0-day delay. The varying time delay makes it difficult to produce a representative MEE precipitation climatology. Information about solar wind speed increases the prediction capabilities for both CMEs and HSSs. However, different speed thresholds need to be applied for the different structures to determine the probability of delay (see Figure 7).

The lower energies in the MEE fluxes are often associated directly with substorm injection. However, the high-energy tail (E3) needs additional energizing (Li et al., 2005; Tyssøy, Partamies, Babu, Smith-Johnsen, & Salice, 2021). Therefore, the physical mechanisms that link solar wind velocity to MEE precipitation are likely to be two-fold. Larger solar wind velocities can produce more intense ULF waves within the magnetosphere (Engebretson et al., 1998), providing radial diffusion and energizing the lower energy electrons (Barker et al., 2005; Schulz & Lanzerotti, 1974). Simultaneously, high solar wind speed is a good predictor of the substorm onset probability (Newell et al., 2016). Substorms will fuel VLF chorus waves, and the injected seed particles can be energized as they drift across the substorm-induced electric field on the night side.

Miyoshi et al. (2013) highlighted the importance of the southward (negative) IMF B_z component in accelerating the high-energy tail of the radiation belt population. Miyoshi et al. (2013) showed that HSS dominated by a southward IMF are associated with large flux enhancements of relativistic electrons. However, the role of B_z in our analysis is less evident due to the daily resolution wherein the average B_z is near zero, as it is likely to have both positive and negative values throughout the day. Nonetheless, as ϵ emphasizes negative B_z values, it will better represent the geoeffectiveness throughout a day which might be relevant in terms of peak flux levels and delay.

The timing of the E3 peaks is a product of both the acceleration processes and the lifetime of the respective electron enhancement. A short delay of zero or 1 day is typically linked to both high E1 values and high solar wind velocity based on Figure 6. This implies that an efficient acceleration process needs to be accompanied by an efficient loss process.

The lifetimes of MEE in the radiation belts depend on the energy, radial distance from Earth, and the level of geomagnetic activity. The lifetimes for 100 keV electrons at a radial distance of about four earth radii from the center of the Earth are approximately 3.6 days and 13 hr for quiet and active geomagnetic conditions, respectively (Orlova et al., 2016). Hence, a short lifetime is likely to follow the strength of the coupling functions, ϵ , which is closely linked to geomagnetic activity (Newell et al., 2016). This link is consistent with the average ϵ values for HSSs in Figure 6, whereas the average ϵ values for CMEs are a bit more ambiguous. The expected lifetime can, however, also be rapidly reduced in the case of magnetopause shadowing, where trapped particles over several radial distances are lost to the magnetopause. Magnetopause shadowing is a consequence of a sudden dynamic pressure increase in the solar wind, alongside convection-driven outward radial transport (D. L. Turner et al., 2012), both commonly associated with CME events.

4.3. Duration

Similar to the flux peaks, the duration of the MEE precipitation events will depend on a combination of the acceleration and loss mechanisms. Figure 8 shows longer flux enhancements of the high-energy tail compared to E1. CMEs have a higher probability for a short E1 duration (62% chance of lasting 1 day) compared to the other structures, which are more likely to be associated with durations of 2 days. Similarly, Longden et al. (2008) found that the mean electron flux intensity for 50–500 keV electrons during geomagnetic storms driven by CMEs typically return to pre-storm levels after 1–2 days from zero epoch (the first minimum in Dst), while CIR-driven

storms do not return to pre-storm values within their 3-day analysis after zero epoch. In our study, all structures, including CMEs, showed that the high-energy tail of the MEE precipitation had the highest probability of lasting 3–5 days, indicating the possibility of strong, long-lasting precipitation of E3 electrons in all structures, including CMEs. The shorter E1 duration associated with CMEs does not appear to suggest a shorter E3 duration. Note that the conclusion about the duration of the flux responses during CMEs is based on a few events but still seems to have a solid trend.

When examining the different solar wind parameters, it was concluded that they have no significant correlation with the duration of the flux responses and were, therefore, not included in this study. Tyssøy, Partamies, Babu, Smith-Johnsen, & Salice (2021) found the >292 keV precipitation fluxes to correlate well with the accumulated geomagnetic activity, assuming a lifetime of 9 days. Hence, the flux response and its duration are likely to be an accumulated effect of the preceding geomagnetic activity. This feature cannot be accounted for in the present analysis focusing on isolated events.

Moreover, Tyssøy et al. (2019) discussed the implication of underestimating the duration of the MEE precipitation events. It is, therefore, essential that an MEE precipitation parameterization applied in chemistry-climate models reflects the variability found in Figure 8.

5. Conclusion

Motivated by the demand to create a MEE parameterization that goes beyond the average picture, this study targets three key aspects needed to understand the high-energy tail of MEE precipitation: peak flux, delay, and duration. MEE precipitation is explored in the context of its solar wind drivers and the associated solar wind properties. The BLC measurements of the E1 (>43 keV) and E3 (>292 keV) MEE fluxes based on the MEPED detectors for the years 2004–2014 (one solar cycle) at 55°–75° CGM latitude are used. These energy channels reflect the general behavior of MEE and its high-energy tail. The key aspects are evaluated concerning the probability of a specific response.

The high occurrence frequency of HSSs compared to CMEs implies that they will strongly dominate the average event throughout a solar cycle in terms of flux strength, the delay of the high-energy tail, and the duration. In this study, HSSs constitute 73% of all 249 events selected in the 11 yr and are found to have lower flux responses than CME and combined events. Hence, the average event will best represent HSSs and underestimate stronger precipitation events.

There is a strong link between the peak fluxes in E1 and E3, with a correlation of 0.89. Information on the delay is needed to utilize their temporal relationship in a model. Moreover, higher correlations can be achieved when considering the respective solar wind driver. ϵ is a good parameter to use if the solar wind structure is unknown as the relation between ϵ and the E3 peak is the same for CMEs and HSSs.

E3 peaks 0–3 days after E1 peaks. The highest probability of ~42% occurs for a 1-day delay, independent of solar wind structure. CMEs and HSS + CMEs have higher probabilities for faster E3 responses (>70% for a zero-one-day delay) compared to the other structures. Considering solar wind speed will increase the capability of predicting the delay for both CMEs and HSSs. Different speed thresholds for the different structures need to be applied.

All structures are associated with longer flux enhancements of the high-energy tail compared to E1. The duration of the E1 response has the highest probability of lasting 1 day for CMEs, whereas there is a higher probability of durations of 2 days for other structures. Nevertheless, the duration of the E3 response has the highest probability of lasting 4 days for both CMEs and HSSs. None of the applied solar wind parameters correlated with the duration of the MEE events.

A future MEE precipitation parameterization should represent the variability on both daily and decadal scales more realistically, allowing a better description of the subsequent atmospheric and chemical impact. This could be achieved by implementing a stochastic MEE parameterization accounting for the range of possible flux responses, delay, and duration. This is particularly important to understand the impact of the high-energy tail of the MEE spectrum.

Data Availability Statement

The NOAA/POES MEPED data used in this study are available from the National Oceanic and Atmospheric Administration (<https://www.ngdc.noaa.gov/stp/satellite/poes/dataaccess.html>). The bounce loss cone fluxes used in this study are available at Zenodo via <https://doi.org/10.5281/zenodo.6590387>. Geomagnetic indices and solar wind parameters were obtained from NASA Omniweb at <https://omniweb.gsfc.nasa.gov/form/dx1.html>.

The authors gratefully acknowledge the SuperMAG collaborators (<https://supermag.jhuapl.edu/info/?page=acknowledgement>) where the epsilon (ϵ) parameter was downloaded.

Acknowledgments

The study is supported by the Norwegian Research Council (NRC) under contracts 223252 and 302040. HNT further acknowledges the Young CAS (Centre for Advanced Studies) fellow program. The authors thank the Space Weather Prediction Center (SWPC), NOAA for providing the MEPED data. IGR acknowledges support from the ACE mission.

References

- Akasofu, S. I. (1981). Energy coupling between the solar wind and the magnetosphere. *Space Science Reviews*, 28(2). <https://doi.org/10.1007/BF00218810>
- Asikainen, T., & Ruopsa, M. (2016). Solar wind drivers of energetic electron precipitation. *Journal of Geophysical Research: Space Physics*, 121(3), 2209–2225. <https://doi.org/10.1002/2015JA022215>
- Babu, E. M., Tyssøy, H. N., Smith-Johnsen, C., Maliniemi, V., Salice, J. A., Millan, R. M., & Richardson, I. G. (2022). Determining latitudinal extent of energetic electron precipitation using MEPED on-board NOAA/POES. *Journal of Geophysical Research: Space Physics*, 127(9). <https://doi.org/10.1029/2022JA030489>
- Baldwin, M. P., & Dunkerton, T. J. (2001). Stratospheric harbingers of anomalous weather regimes. *Science*, 294(5542), 581–584. <https://doi.org/10.1126/science.1063315>
- Barker, A. B., Li, X., & Selesnick, R. S. (2005). Modeling the radiation belt electrons with radial diffusion driven by the solar wind. *Space Weather*, 3(10). <https://doi.org/10.1029/2004SW000118>
- Beharrell, M. J., Honary, F., Rodger, C. J., & Chilver, M. A. (2015). Substorm-induced energetic electron precipitation: Morphology and prediction. *Journal of Geophysical Research: Space Physics*, 120(4), 2993–3008. <https://doi.org/10.1002/2014JA020632>
- Borovsky, J. E., & Denton, M. H. (2006). Differences between CME-driven storms and CIR-driven. *Journal of Geophysical Research: Space Physics*, 111(A7), A07S08. <https://doi.org/10.1029/2005JA011447>
- Damiani, A., Funke, B., López-Puertas, M., Santee, M. L., Cordero, R. R., & Watanabe, S. (2016). Energetic particle precipitation: A major driver of the ozone budget in the Antarctic upper stratosphere. *Geophysical Research Letters*, 43(7), 3554–3562. <https://doi.org/10.1002/2016GL068279>
- Duderstadt, K. A., Huang, C.-L., Spence, H. E., Smith, S., Blake, J. B., Crew, A. B., et al. (2021). Estimating the impacts of radiation belt electrons on atmospheric chemistry using FIREBIRD II and Van Allen Probes observations. *Journal of Geophysical Research: Atmospheres*, 126(7). <https://doi.org/10.1029/2020JD033098>
- Engebretson, M., Glassmeier, K.-H., Stellmacher, M., Hughes, W. J., & Lühr, H. (1998). The dependence of high-latitude PcS wave power on solar wind velocity and on the phase of high-speed solar wind streams. *Journal of Geophysical Research: Space Physics*, 103(A11), 26271–26283. <https://doi.org/10.1029/97JA03143>
- Evans, D. S., & Greer, M. S. (2004). Polar orbiting environmental satellite space environment monitor - 2: Instrument descriptions and archive data documentation. NOAA Technical Memorandum version 1.4.
- Funke, B., Baumgaertner, A., Calisto, M., Egorova, T., Jackman, C. H., Kieser, J., et al. (2011). Composition changes after the “Halloween” solar proton event: The High Energy Particle Precipitation in the Atmosphere (HEPPA) model versus MIPAS data intercomparison study. *Atmospheric Chemistry and Physics*, 11(17), 9089–9139. <https://doi.org/10.5194/acp-11-9089-2011>
- Gjerloev, J. W. (2012). The SuperMAG data processing technique. *Journal of Geophysical Research*, 117(A9). <https://doi.org/10.1029/2012JA017683>
- Hendrickx, K., Megner, L., Gumbel, J., Siskind, D. E., Orsolini, Y. J., Tyssøy, H. N., & Hervig, M. (2015). Observation of 27 days solar cycles in the production and mesospheric descent of EPP-produced NO. *Journal of Geophysical Research: Atmospheres*, 120(10), 8978–8988. <https://doi.org/10.1002/2015JA021441>
- Horne, R. B., Thorne, R. M., Glauert, S. A., Albert, J. M., Meredith, N. P., & Anderson, R. R. (2005). Timescale for radiation belt electron acceleration by whistler mode chorus waves. *Journal of Geophysical Research*, 110(A3), A03225. <https://doi.org/10.1029/2004JA010811>
- Jackman, C. H., DeLand, M. T., Labow, G. J., Fleming, E. L., Weisenstein, D. K., Ko, M. K. W., & Russell, J. M. (2005). Neutral atmospheric influences of the solar proton events in October–November 2003. *Journal of Geophysical Research*, 110(A9). <https://doi.org/10.1029/2004ja010888>
- Kataoka, R., & Miyoshi, Y. (2006). Flux enhancement of radiation belt electrons during geomagnetic storms driven by coronal mass ejections and corotating interaction regions. *Space Weather*, 4(9). <https://doi.org/10.1029/2005SW000211>
- Kennel, C. F., & Petschek, H. E. (1966). Limit on stably trapped particle fluxes. *Geophysical Research*, 71, 1–28. <https://doi.org/10.1029/JZ071i001p00001>
- Kidston, J., Scaife, A. A., Hardiman, S. C., Mitchell, D. M., Butchart, N., Baldwin, M. P., & Gray, L. J. (2015). Stratospheric influence on tropospheric jet streams, storm tracks, and surface weather. *Nature Geoscience*, 8(6), 433–440. <https://doi.org/10.1038/ngeo2424>
- Kilpua, E. K. J., Balogh, A., von Steiger, R., & Liu, Y. D. (2017). Geoeffective properties of solar transients and stream interaction regions. *Space Science Reviews*, 212(3–4), 1271–1314. <https://doi.org/10.1007/s11214-017-0411-3>
- Kilpua, E. K. J., Koskinen, H. E. J., & Pulkkinen, T. I. (2017). Coronal mass ejections and their sheath regions in interplanetary space. *Living Reviews in Solar Physics*, 14(1), 5. <https://doi.org/10.1007/s41116-017-0009-6>
- Koskinen, H. E. J., & Tanskanen, E. I. (2002). Magnetospheric energy budget and the epsilon parameter. *Journal of Geophysical Research: Space Physics*, 107(A11), 1415. <https://doi.org/10.1029/2002JA009283>
- Li, X., Baker, D. N., Temerin, M., Reeves, G., Friedel, R., & Shen, C. (2005). Energetic electrons, 50 keV to 6 MeV, at geosynchronous orbit: Their responses to solar wind variations. *Space Weather*, 3(4). <https://doi.org/10.1029/2004SW000105>
- Longden, N., Denton, M. H., & Honary, F. (2008). Particle precipitation during ICME-driven and CIR-driven geomagnetic storms. *Journal of Geophysical Research*, 113(A6). <https://doi.org/10.1029/2007JA012752>
- Maliniemi, V., Asikainen, T., & Mursula, K. (2016). Effect of geomagnetic activity on the northern annular mode: QBO dependence and the Holton-Tan relationship. *Journal of Geophysical Research: Atmospheres*, 121(17), 10043–10055. <https://doi.org/10.1002/2015JD024460>
- Maliniemi, V., Nesse Tyssøy, H., Smith-Johnsen, C., Arsenovic, P., & Marsh, D. R. (2021). Effects of enhanced downwelling of NO_x on Antarctic upper-stratospheric ozone in the 21st century. *Atmospheric Chemistry and Physics*, 21(14), 11041–11052. <https://doi.org/10.5194/acp-21-11041-2021>
- Marsh, D., Solomon, S., & Reynolds, A. (2004). Empirical model of nitric oxide in the lower thermosphere. *Journal of Geophysical Research*, 109(A7), A07301. <https://doi.org/10.1029/2003ja010199>
- Matthes, K., Funke, B., Andersson, M. E., Barnard, L., Beer, J., Charbonneau, P., et al. (2017). Solar forcing for CMIP6. *Geoscientific Model Development*, 10(6), 2247–2302. <https://doi.org/10.5194/gmd-10-2247-2017>
- Millan, R. M., & Thorne, R. M. (2007). Review of radiation belt relativistic electron losses. *Journal of Atmospheric and Solar-Terrestrial Physics*, 69(3), 362–377. <https://doi.org/10.1016/j.jastp.2006.06.019>
- Mironova, I. A., Artamonov, A. A., Bazilevskaya, G. A., Rozanov, E. V., Kovaltsov, G. A., Makhmutov, V. S., et al. (2019). Ionization of the polar atmosphere by energetic electron precipitation retrieved from balloon measurements. *Geophysical Research Letters*, 46(2), 990–996. <https://doi.org/10.1029/2018GL079421>

- Miyoshi, Y., Kataoka, R., Kasahara, Y., Kumamoto, A., Nagai, T., & Thomsen, M. F. (2013). High-speed solar wind with southward interplanetary magnetic field causes relativistic electron flux enhancement of the outer radiation belt via enhanced condition of whistler waves. *Geophysical Research Letters*, *40*(17), 4520–4525. <https://doi.org/10.1002/grl.50916>
- Newell, P., Liou, K., Gjerloev, J., Sotirelis, T., Wing, S., & Mitchell, E. (2016). Substorm probabilities are best predicted from solar wind speed. *Journal of Atmospheric and Solar-Terrestrial Physics*, *146*, 28–37. <https://doi.org/10.1016/j.jastp.2016.04.019>
- Ødegaard, L.-K. G., Tyssøy, H. N., Søråas, F., Stadsnes, J., & Sandanger, M. I. (2017). Energetic electron precipitation in weak to moderate corotating interaction region driven storms. *Journal of Geophysical Research: Space Physics*, *122*(3), 2900–2921. <https://doi.org/10.1002/2016JA023096>
- Orlova, K., Shprits, Y., & Spasojevic, M. (2016). New global loss model of energetic and relativistic electrons based on Van Allen Probes measurements. *Journal of Geophysical Research: Space Physics*, *121*(2), 1308–1314. <https://doi.org/10.1002/2015JA021878>
- Østgaard, N., Vondrak, R. R., Gjerloev, J. W., & Germany, G. (2002). A relation between the energy deposition by electron precipitation and geomagnetic indices during substorms. *Journal of Geophysical Research*, *107*(A9), 1246. <https://doi.org/10.1029/2001JA002003>
- Partamies, N., Tesema, F., Bland, E., Heino, E., Nesse Tyssøy, H., & Kallelid, E. (2021). Electron precipitation characteristics during isolated, compound, and multi-night substorm events. *Annales Geophysicae*, *39*(1), 69–83. <https://doi.org/10.5194/angeo-39-69-2021>
- Pettit, J., Randall, C., Peck, E., Marsh, D., van de Kamp, M., Fang, X., et al. (2019). Atmospheric effects of >30 keV energetic electron precipitation in the Southern Hemisphere winter during 2003. *Journal of Geophysical Research: Space Physics*, *124*(10), 8138–8153. <https://doi.org/10.1029/2019JA026868>
- Richardson, I. G. (2018). Solar wind stream interaction regions throughout the heliosphere. *Living Reviews in Solar Physics*, *15*(1), 1. <https://doi.org/10.1007/s41116-017-0011-z>
- Richardson, I. G., & Cane, H. V. (2012). Near-Earth solar wind flows and related geomagnetic activity during more than four solar cycles (1963–2011). *Journal of Space Weather and Space Climate*, *2*, A02. <https://doi.org/10.1051/swsc/2012003>
- Rodger, C., Clilverd, M. A., Green, J. C., & Lam, M. M. (2010). Use of POES SEM-2 observations to examine radiation belt dynamics and energetic electron precipitation into the atmosphere. *Journal of Geophysical Research*, *115*(A4). <https://doi.org/10.1029/2008JA014023>
- Schulz, M., & Lanzerotti, L. J. (1974). *Particle diffusion in the radiation belts*. Springer.
- Seppälä, A., Randall, C. E., Clilverd, M. A., Rozanov, E., & Rodger, C. J. (2016). Geomagnetic activity and polar surface air temperature variability. *Journal of Geophysical Research*, *114*(A10). <https://doi.org/10.1029/2008JA014029>
- Sinnhuber, M., Kazeminejad, S., & Wissing, J. M. (2011). Interannual variation of NO_x from the lower thermosphere to the upper stratosphere in the years 1991–2005. *Journal of Geophysical Research*, *116*(A2). <https://doi.org/10.1029/2010ja015825>
- Sinnhuber, M., Nesse Tyssøy, H., Asikainen, T., Bender, S., Funke, B., Hendrickx, K., et al. (2022). Heppa III intercomparison experiment on electron precipitation impacts: 2. Model-measurement intercomparison of nitric oxide (NO) during a geomagnetic storm in April 2010. *Journal of Geophysical Research: Space Physics*, *127*(1). <https://doi.org/10.1029/2021JA029466>
- Smith-Johnsen, C., Tyssøy, H. N., Hendrickx, K., Orsolini, Y., Kumar, G. K., Ødegaard, L.-K. G., et al. (2017). Direct and indirect electron precipitation effect on nitric oxide in the polar middle atmosphere, using a full-range energy spectrum. *Journal of Geophysical Research: Space Physics*, *122*(8), 8679–8693. <https://doi.org/10.1002/2017JA024364>
- Solomon, S., Crutzen, P. J., & Roble, R. G. (1982). Photochemical coupling between the thermosphere and the lower atmosphere: 1. Odd nitrogen from 50 to 120 km. *Journal of Geophysical Research*, *87*(C9), 7206–7220. <https://doi.org/10.1029/JC087iC09p07206>
- Theodoridis, G. C., & Paolini, F. R. (1967). Pitch angle diffusion of relativistic outer belt electrons. *Annales Geophysicae*, *23*, 375–381.
- Turner, D. L., Shprits, Y., Hartinger, M., & Angelopoulos, V. (2012). Explaining sudden losses of outer radiation belt electrons during geomagnetic storms. *Nature Physics*, *8*(3), 208–212. <https://doi.org/10.1038/nphys2185>
- Turner, N. E., Cramer, W. D., Earles, S. K., & Emery, A. B. (2009). Geoefficiency and energy partitioning in CIR-driven and CME-driven storms. *Journal of Atmospheric and Solar-Terrestrial Physics*, *71*(10–11), 1023–1031. <https://doi.org/10.1016/j.jastp.2009.02.005>
- Turunen, E., Verronen, P. T., Seppälä, A., Rodger, C. J., Clilverd, M. A., Tamminen, J., et al. (2009). Impact of different energies of precipitating particles on NO_x generation in the middle and upper atmosphere during geomagnetic storms. *Journal of Atmospheric and Solar-Terrestrial Physics*, *71*(10–11), 1176–1189. <https://doi.org/10.1016/j.jastp.2008.07.005>
- Tyssøy, H. N., Haderlein, A., Sandanger, M. I., & Stadsnes, J. (2019). Intercomparison of the POES/MEPED loss cone electron fluxes with the CMIP6 parametrization. *Journal of Geophysical Research: Space Physics*, *124*(1), 628–642. <https://doi.org/10.1029/2018JA025745>
- Tyssøy, H. N., Partamies, N., Babu, E. M., Smith-Johnsen, C., & Salice, J. A. (2021). The predictive capabilities of the auroral electrojet index for medium energy electron precipitation. *Frontiers in Astronomy and Space Sciences*, *8*. <https://doi.org/10.3389/fspas.2021.714146>
- Tyssøy, H. N., Sandanger, M. I., Ødegaard, L. G., Stadsnes, J., Aasnes, A., & Zawedde, A. E. (2016). Energetic electron precipitation into the middle atmosphere—Constructing the loss cone fluxes from MEPED POES. *Journal of Geophysical Research: Space Physics*, *121*(6), 5693–5707. <https://doi.org/10.1002/2016JA022752>
- Tyssøy, H. N., Sinnhuber, M., Asikainen, T., Bender, S., Clilverd, M. A., Funke, B., et al. (2021). HEPPA III intercomparison experiment on electron precipitation impacts: 1. Estimated ionization rates during a geomagnetic active period in April 2010. *Journal of Geophysical Research: Space Physics*, *127*. <https://doi.org/10.1029/2021JA029128>
- Tyssøy, H. N., & Stadsnes, J. (2015). Cutoff latitude variation during solar proton events: Causes and consequences. *Journal of Geophysical Research: Space Physics*, *120*(1), 553–563. <https://doi.org/10.1002/2014JA020508>
- Tyssøy, H. N., Stadsnes, J., Søråas, F., & Sørbø, M. (2013). Variations in cutoff latitude during the January 2012 solar proton event and implication for the distribution of particle energy deposition. *Geophysical Research Letters*, *40*(16), 4149–4153. <https://doi.org/10.1002/grl.50815>
- van de Kamp, M., Rodger, C. J., Seppälä, A., Clilverd, M. A., & Verronen, P. T. (2018). An updated model providing long-term data sets of energetic electron precipitation, including zonal dependence. *Journal of Geophysical Research: Atmospheres*, *123*(17), 9891–9915. <https://doi.org/10.1029/2017JD028253>
- van de Kamp, M., Seppälä, A., Clilverd, M. A., Rodger, C. J., Verronen, P. T., & Whittaker, I. C. (2016). A model providing long-term data sets of energetic electron precipitation during geomagnetic storms. *Journal of Geophysical Research: Atmospheres*, *121*(20), 12520–12540. <https://doi.org/10.1002/2015JD024212>
- Verronen, P. T., & Lehmann, R. (2013). Analysis and parameterization of ionic reactions affecting middle atmospheric HO_x and NO_y during solar proton events. *Annales Geophysicae*, *31*(5), 909–956. <https://doi.org/10.5194/angeo-31-909-2013>
- Verronen, P. T., Seppälä, A., Kyrölä, E., Tamminen, J., Pickett, H. M., & Turunen, E. (2006). Production of odd hydrogen in the mesosphere during the January 2005 solar proton event. *Geophysical Research Letters*, *33*(24), L24811. <https://doi.org/10.1029/2006GL028115>
- (WCRP), W. C. R. P. (2011). WCRP Coupled Model Intercomparison Project (CMIP). Retrieved from <https://www.wcrp-climate.org/wgcm-cmip>
- Yando, K., Millan, R. M., Green, J. C., & Evans, D. S. (2011). A Monte Carlo simulation of the NOAA POES medium energy proton and electron detector instrument. *Journal of Geophysical Research: Space Physics*, *116*(A10). <https://doi.org/10.1029/2011JA016671>

- Zawedde, A. E., Tyssøy, H. N., Stadsnes, J., & Sandanger, M. I. (2018). The impact of energetic particle precipitation on mesospheric OH—Variability of the sources and the background atmosphere. *Journal of Geophysical Research: Space Physics*, *123*(7), 5764–5789. <https://doi.org/10.1029/2017JA025038>
- Zhang, J., Richardson, I. G., Webb, D. F., Gopalswamy, N., Huttunen, E., Kasper, J. C., et al. (2007). Solar and interplanetary sources of major geomagnetic storms ($Dst \leq -100$ nT) during 1996–2005. *Journal of Geophysical Research*, *112*(A10). <https://doi.org/10.1029/2007JA012321>
- Zhang, Y., & Paxton, L. (2008). An empirical Kp -dependent global auroral model based on TIMED/GUVI FUV data. *Journal of Atmospheric and Solar-Terrestrial Physics*, *70*(8–9), 1231–1242. <https://doi.org/10.1016/j.jastp.2008.03.008>
- Zurbuchen, T. H., & Richardson, I. G. (2006). In-situ solar wind and magnetic field signatures of interplanetary coronal mass ejections. *Space Science Reviews*, *123*(1–3), 31–43. <https://doi.org/10.1007/s11214-006-9010-4>